

Molecular Architecture of PSMa1 Functional Amyloids

Paolo Elvati

University of Michigan <https://orcid.org/0000-0002-6882-6023>

Chloe Luyet

University of Michigan <https://orcid.org/0000-0002-1772-8618>

Yichun Wang

University of Notre Dame

Changjiang Liu

University of Michigan <https://orcid.org/0000-0003-3272-0689>

J VanEpps

University of Michigan-Ann Arbor <https://orcid.org/0000-0002-0805-0913>

Nicholas Kotov

University of Michigan <https://orcid.org/0000-0002-6864-5804>

Angela Violi (✉ avioli@umich.edu)

University of Michigan

Article

Keywords:

Posted Date: February 8th, 2022

DOI: <https://doi.org/10.21203/rs.3.rs-1273003/v1>

License:  This work is licensed under a Creative Commons Attribution 4.0 International License.

[Read Full License](#)

Molecular Architecture of PSM α 1 Functional Amyloids

Paolo Elvati^{1,†}, Chloe Luyet^{2,†}, Yichun Wang^{2,3,†}, Changjiang Liu⁴, J. Scott VanEpps^{5,6,7,8,9}, Nicholas Kotov^{2,*}, and Angela Violi^{1,2,*}

¹Mechanical Engineering, University of Michigan, Ann Arbor, 48108, USA

²Chemical Engineering, University of Michigan, Ann Arbor, 48108, USA

³Chemical and Biomolecular Engineering, University of Notre Dame, Notre Dame, Indiana, 46556, United States

⁴Biophysics, University of Michigan, Ann Arbor, 48108, USA

⁵Biointerfaces Institute, University of Michigan, Ann Arbor, Michigan 48109, United States

⁶Emergency Medicine, University of Michigan, Ann Arbor, MI, USA

⁷Biomedical Engineering, University of Michigan, Ann Arbor, MI, USA

⁸Macromolecular Science and Engineering, University of Michigan, Ann Arbor, MI, USA

⁹Michigan Center for Integrative Research in Critical Care, University of Michigan, Ann Arbor, MI, USA

*To whom correspondence should be addressed: kotov@umich.edu, avioli@umich.edu

†These authors contributed equally to this work

ABSTRACT

Biofilms are structurally and functionally complex networks of bacteria and nanoscale macromolecules that play an important role in a myriad of settings from personal health and agriculture to power productions and fuel storage. Amyloid nanofibers are integral components of many biofilms and serve various purposes ranging from virulent to structural. Nonetheless, the precise characterization of bacterial amyloid nanofibers has been elusive, with incomplete and contradicting results. The present work focuses on the molecular details and characteristics of PSM α 1-derived functional amyloids present in *Staphylococcus aureus* biofilms, using a combination of computational and experimental techniques. Results from molecular dynamics simulations, guided and supported by a variety of experiments, show that nanoscale nanofibers present a helical structure formed by two-protofilament PSM α 1 amyloid nanofibers. PSM α 1 peptides assemble into cross- β -sheet structures with an average diameter of about 12 nm, adopting a left-handed helical structure with a periodicity of approximately 72 nm. Strikingly, the chirality of the self-assembled nanofibers, an intrinsic geometric property of its constituent peptides, is central in determining the growth and shape of the fibers. The presented findings provide structural insights into the properties of the functional amyloids, hypothesize the role of chirality on the formation of fibers, and aid in strategies for the design of anti-amyloid compounds.

Main

Bacterial biofilms are communities of single or multiple species of microorganisms, attached to a surface and organized into a complex three-dimensional structure^{1,2}. To form a functional structure, biofilm cells produce polymers that constitute the extracellular matrix (ECM), which facilitates binding between cells and to the surface. The most extensively studied components of biofilm ECMs are polysaccharides, nucleic acids, and proteins, but the relative amounts of these compounds vary depending on the species^{3,4}. A major protein component of the ECM are peptides that form amyloid nanoscale fibrils, which are highly resistant to chemical and enzymatic degradation, providing a strong scaffold for the bacterial community^{5–7}.

Some amyloids are functional, in that they participate in physiological activities: they can act as toxins, killing non-self-cells, or they can operate as a physical barrier in biofilms, increasing resilience and resistance to antimicrobial drugs and immune mediators^{8–12}. Functional amyloids are known for their stability attributed to their cross- β structure, which includes parallel β -sheet strands that run parallel to the nanofiber axis and peptide pairs that aggregate perpendicular to the nanofiber axis^{7,8,12–16}.

The presence of these nanofibers is extremely common in bacterial biofilms. They have been identified in Chloroflexi, Actinobacteria, Bacteroidetes, Firmicutes, and Proteobacteria¹⁷. Within the Firmicutes phylum, *Staphylococcus aureus* is a well-known pathogenic, Gram-positive bacterium that generates extensive biofilm structures. In the United States, infections associated with *S. aureus* have an estimated mortality rate of 25% (higher in the case of drug-resistant strains), causing a high number of hospitalizations and significant medical costs¹⁸. Indeed, mortality caused by methicillin-resistant *S. aureus* (MRSA) remains the highest for any antibiotic-resistant pathogen, reported by the CDC to be at ~20,000 in 2018¹⁹. The significance of the problem has been exacerbated by the COVID-19 pandemic due to frequency of bacterial superinfection²⁰.

Staphylococcal species possess a specific set of amyloid-forming peptides known as phenol soluble modulins (PSMs) that

serve as key virulence factors that stimulate inflammatory responses, alter the host cell cycle, lyse human cells, and contribute to biofilm structuring^{21–23}. PSMs, α -helical amphiphatic peptides, are classified depending on their length. The smallest peptides (21 amino acids in length) are α -type, PSM α 1–4 and δ -toxin. The longer peptides, which are 44 amino acids in length, are PSM β 1 and PSM β 2. Despite their sequence similarity, not all PSMs form ordered amyloid structures and not all of them follow the same structural motifs. As such, PSM α 3, the most toxic member, forms cross- α nanofibrils, while PSM α 1 and PSM α 4 form canonical cross- β amyloid nanofibers. A truncated PSM α 3 instead presents atypical β -rich nanofibril architectures, highlighting the importance of structure as basis of functional diversity exhibited by *S. aureus* PSM α s²⁴.

To date, various open questions remain about the formation and characteristics of PSM-derived amyloid nanofibers. Some studies have identified the crystal structures of functional amyloids reporting a consistent nanofiber diameter of approximately 10–12 nm^{25,26}, but a specific reason for this mechanism of growth has not been completely deciphered. Similarly, the chirality and helical structure of the nanofibers remains controversial^{13,24}. From an experimental perspective, a critical issue is that large insoluble biological complexes, like PSM nanofibers, reaching microns in length^{27,28}, are difficult to crystallize²⁹. Moreover, structures obtained from crystals are not necessarily accurate representations of the nanofibers in dispersions, as the conditions that promote crystallization may differ substantially from typical *in vivo* and *in vitro* experimental environments, and even in solution. Finally, the formation of amyloid nanofibers is a relatively slow process that can take from a few days *in vitro*^{26,30} to more than a week in solution³¹. Most aspects of this transition are still unclear and are further complicated *in vitro* by the interactions with other biomacromolecules present in the ECM, like extracellular DNA³⁰ and other peptides (*e.g.*, the N-terminus of the quorum sensing signal peptide AgrD)^{32,33}. The slow and gradual transition from single peptide to amyloid nanofibers suggests a process that involves configurational and conformational transformations with several relatively stable intermediates, which are unlikely to be captured by crystallographic experiments³⁴. The dynamics between labile bonds, equilibrium conformations, soluble and insoluble states, even with identical sequences, challenge structure-function-fibrillation studies. There is, therefore, a clear need to gain additional insights on the structures of PSM α 1 functional amyloid nanofibers.

In the present study, we report on the molecular structure of PSM α 1 nanofibers and their characteristics, such as diameter, chirality and periodicity, and advance hypotheses on the role of chirality on the mechanisms of nanofiber assembly. Leveraging a combination of fully-atomistic molecular dynamics (MD) simulations and experimental data obtained via mass spectroscopy and microscopy-based techniques, we probe the characteristics of several *in silico* candidate structures for the amyloid nanofibers.

We find compelling evidence that a cross- β -sheet two-protofilament (2 β) structure is the most plausible structural model for PSM α 1 nanofibers in solution, that matches the experimental values of chirality, diameter, and periodicity of mature PSM α 1 nanofibers in solution.

The presence of randomly coiled amorphous-like regions at the interface of nanofibers and water and between fibers further support the importance of molecular simulations, as rigid crystal structures would fail to capture the entropic and imperfect features of disordered regions of otherwise highly-ordered nanofibers³⁵. After all, amorphous aggregates are a ubiquitous facet in the formation of amyloid nanofibers, characteristic of those in Alzheimer's disease^{13,36,37}, Parkinson's disease, prion misfolding³⁸, and *E. coli* curli^{39–41}, to name a few. Consequently, other amyloid nanofibers should be subject to similar scrutiny by MD simulations of different types^{35,42,43}.

Finally, results from this work open the door to the possibility of designing anti-amyloid nanoparticles⁴⁴ that present specific supramolecular interactions with the nanofibers. The 2 β PSM α 1 amyloid nanofiber model can be used to study nanofiber-antimicrobial interactions to elucidate a mechanism for biofilm manipulation⁴⁴ using man-made biomimetic nanostructures.

Nanofiber Formation and Evolution

As mentioned before, confounding factors (*e.g.*, extracellular DNA) complicate the analysis of PSM α 1 aggregates when formed in *in vitro* biofilm cultures. For this reason, in this work we chose to study the formation of amyloid nanofibers from PSM α 1 aqueous solution. Even without any external direction, promotion, or catalytic induction, PSM α 1 self-assembles into amyloid nanofibers at high concentrations^{26,30,45,46}. Similar to results reported in the literature^{24,44}, in our samples, PSM α 1 nanofibers are detected as early as day 4, *via* β -sheets signal in circular dichroism (CD) spectroscopy (Fig. S1 in SI), and visualized at day 9 *via* transmission electron microscopy (TEM; Fig. S2 in SI); however, the process is longer than previously reported³¹. Fibers keep evolving for about two more weeks: CD spectra taken for samples older than 14 days are characterized by strong β -sheets and disordered structures signals, while diameters measured from TEM images show a significant decrease in the standard error of the mean diameters (Fig. S3 and Tab. S1 in SI) for samples taken at day 21 and later. Leveraging this gradual stabilization, in the following discussion, we will only analyze data of the mature fiber (*i.e.*, after day 14).

The mature PSM α 1 amyloid nanofibers are stable when subjected to thermal and mechanical (*i.e.*, sonication) stress (see Methodology for details), with no discernible change in TEM morphology following these treatments (Fig. S4 in SI). This stability, however, is not the result of a polymerization mechanism in which covalent bonds are formed between peptides, since mass spectroscopy never detects the presence of anything but individual PSM α 1 peptides (Fig. S5 in SI), and the nanofibers can be dissolved with hexafluoroisopropanol (HFIP) and trifluoroacetic acid (TFA) (Fig. 2g).

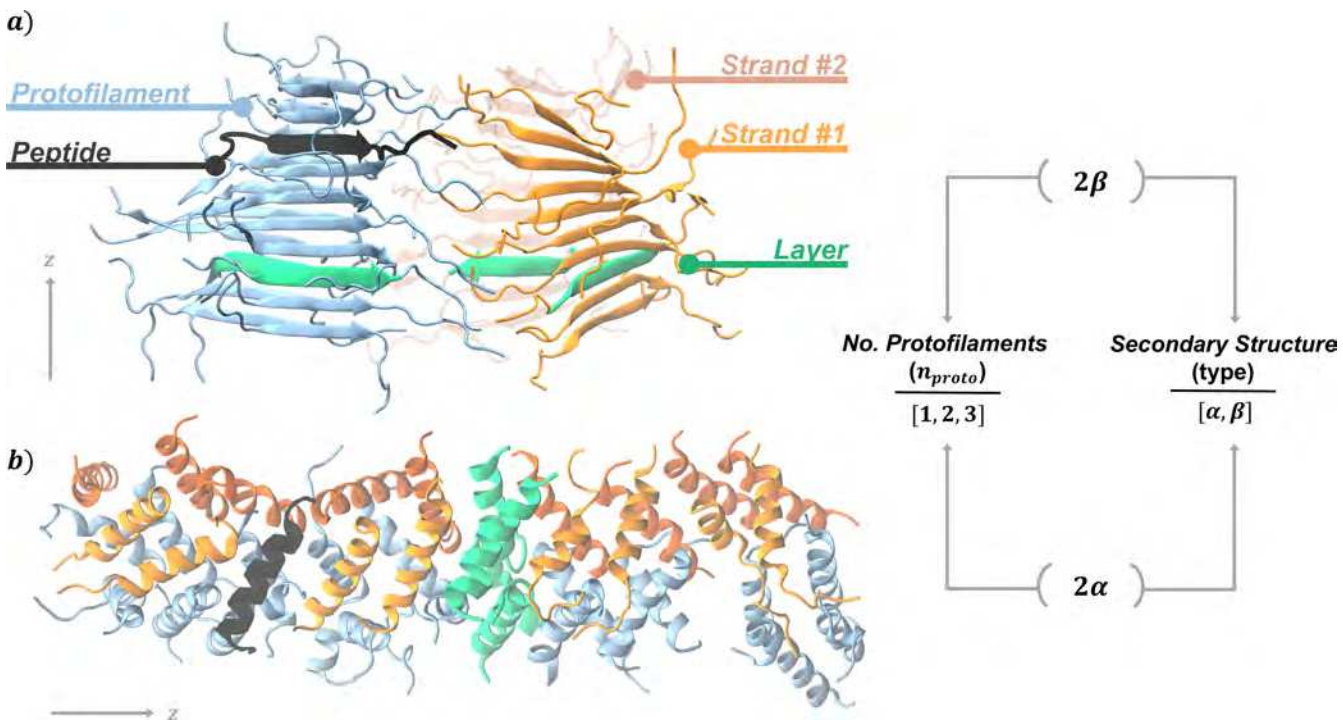


Figure 1. Examples of a PSM α 1 (a) 2β and (b) 2α nanofibers in water, with colors and text illustrating the terminology and labels used in this work. Individual PSM α 1 peptides (black) form long β -strands that pair (*e.g.*, light and dark orange) to form protofilaments (blue). When computing properties, it is convenient to define a layer (green), which is composed of PSM α 1 from different strands and different protofilaments, approximately on a plane perpendicular to the nanofiber axis of elongation. The first character in each nanofiber name (1, 2, 3) represents the number of protofilaments in the structure; the second term (α or β) describes the main structural motif of each peptide molecule within the nanofiber.

Based on these data and the information available in existing literature, we selected six classes of deformed-PSM α 1 aggregates as plausible candidates for the amyloid nanofibers (see Tab. 1). Namely, we simulated aggregates formed by one, two, or three laterally-aggregated protofilaments (Fig. 1 for clarifications regarding terminology) of PSM α 1 in either α -helical or β -sheet configuration, and estimated their characteristics by performing classical all-atom MD simulations. This approach is more time consuming than starting from an experimentally-estimated structure, which is what is generally done for non-bacterial amyloids, but it avoids introducing any bias due to measurement limitations (*e.g.*, crystallization). The α -helical secondary structure was chosen because single PSM α 1 peptides in solution adopt this configuration, while β -sheet structure is the one generally observed for PSM α 1 amyloid nanofibers. For each class, we considered different systems, varying the length of the fiber to account for size limitation of the simulations, under conditions close to the experiments in solution (310 K, NaCl 0.15 M solution). A complete list of the simulated nanofibers can be found in the SI (Fig. S6).

101 Peptide interactions

Simulated nanofibers assembled with α - and β -motifs share only limited similarities. Both types of aggregates are stabilized by a combination of hydrogen bonding, hydrophobic, hydrophilic, and Coulombic interactions, but where these interactions occur differentiates the two types of aggregates (Fig. 2). Within each protofilament, the PSM α 1 peptides of β -sheet nanofibers assemble into parallel β -sheet strands (Fig. 2a), with hydrogen bonds primarily occurring between residues seven through thirteen. By contrast, the peptides in the α -nanofibers do not form hydrogen bonds with other peptides, but rather within each peptide (Fig. 2b). The resulting α nanofibers are weakly stabilized. During the simulations, long aggregates break into smaller clusters, indicating that α -helical peptides are unlikely to form stable assemblies in the absence of external factors. This difference in stability is consistent with the characteristics of the strand interactions. In the α -nanofibers, the peptides orient themselves to form a hydrophobic core (Fig. 2d), while the β -strands within each protofilament are connected through a steric zipper formed by 3–5 hydrophobic amino acids (isoleucine, valine and sometimes glycine, *e.g.*, Fig. 2c). The resulting hydrophobic core for each β -sheet protofilament, an approximately 0.6 nm-radius cylindrical region, is smaller than the elliptical region observed for α nanofibers (approximately 2.5 by 1.5 nm for 1 α , 2.5 by 3.5 nm for 2 α , and 2.5 by 4.5 nm for 3 α).

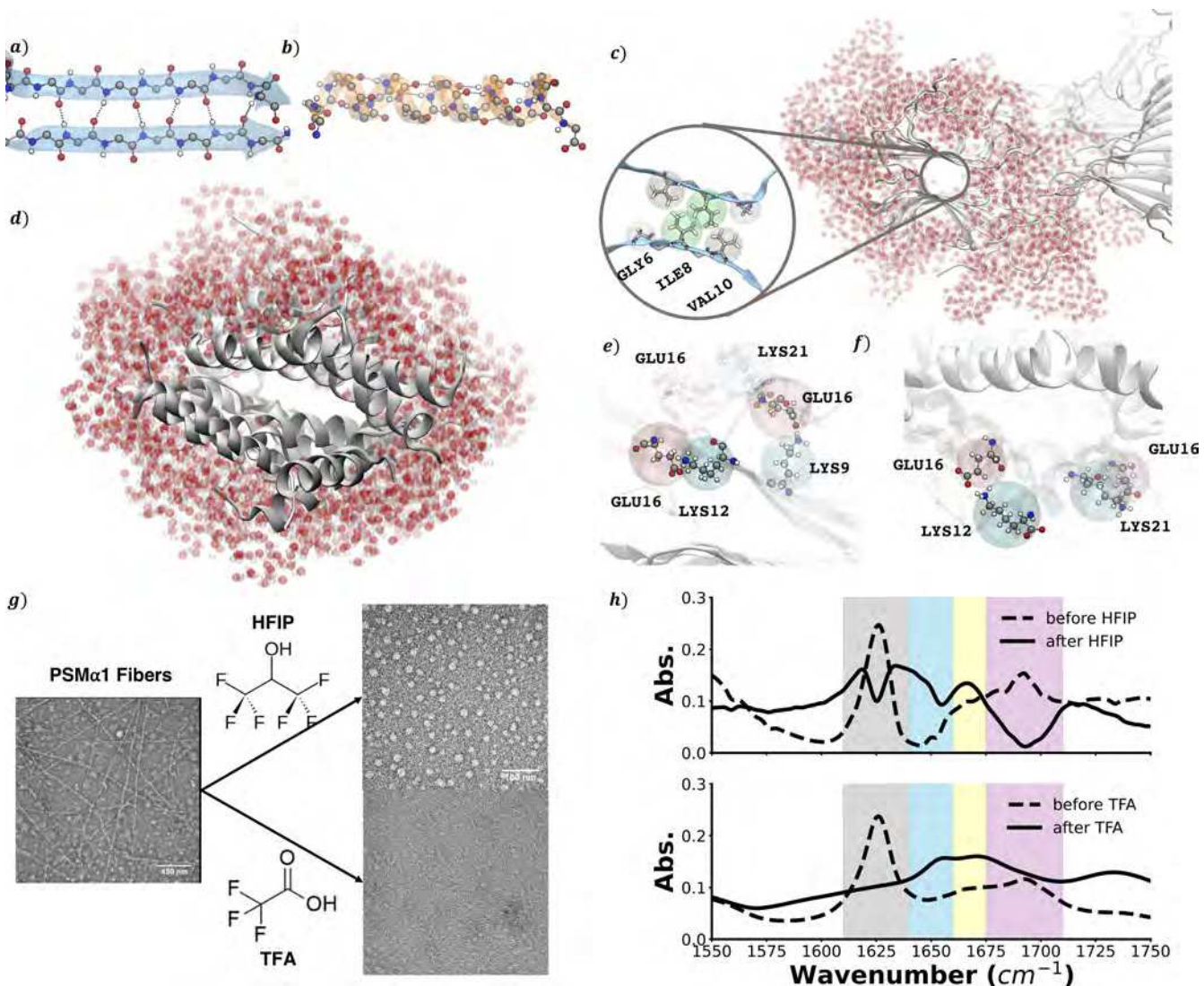


Figure 2. Anatomy of PSM α 1 nanofibers and their interactions. Hydrogen bonds (black dotted lines) stabilize (a) β -sheet strands and (b) α -helices. Hydrophobic regions in (c) β -sheet nanofibers occur inside each protofilament at a 4-to-6-residue steric zipper, and in (d) α -sheet nanofibers between protofilaments; water atoms in the nanofiber's proximity are shown in red. Salt bridges between GLU16 (pink bubbles) and LYS9, LYS12, or LYS21 (cyan bubbles) are found in (e) β and (f) α nanofibers. (g) TEM images of PSM α 1 nanofibers in solution pre- and post-treatment with HFIP and TFA. (h) Fourier-transform infrared spectroscopy of pre- and post- TFA and HFIP treatments. The pre-treated secondary structures of mature nanofibers are primarily β -sheets (1600 cm^{-1} to 1625 cm^{-1}) and β -turns (1700 cm^{-1}), where shaded regions are associated with β -sheet (gray), disordered/random-coil (blue), α -helical (yellow), and β -turn (purple) secondary structures.

The structures of multi-protofilament nanofibers are also very different: α -protofilaments aggregate in assemblies with a common hydrophobic core but different diameter, while β -protofilaments stretch side-by-side, forming locally planar structures. This behavior can be linked to the distribution of charged groups and salt bridges (a bond between the oxygen atoms of an acidic residue and the nitrogen atoms of basic residue). Salt bridges form between residue 16 (glutamic acid) and one of three lysine residues (9, 12, or 21) in both α and β aggregates, as shown in Fig. 2e & f, with differences, however, in both orientation and most likely participating lysine. In the β -sheet nanofibers, the most common salt bridges form with LYS9 (and partially with LYS12), which is located between the residues making up the steric zipper (ILE8 and VAL10), easily accessible to GLU16. By contrast, the salt bridges in α -sheet nanofibers are predominantly formed with LYS12 and LYS21, as LYS9 is part of the α -helix backbone and, therefore, not as readily available.

Our experiments indicate that the simulated β -structures are in better agreement with the characteristics of the β -nanofibers, as infrared spectroscopy shows a strong signal associated with β -sheets and β -turns (Fig. 2g & h). Additionally, treating

126 the mature nanofiber with HFIP, an aprotic surfactant, does not result in a complete nanofiber dissolution and only a partial
 127 disappearance of the β -sheets signal, which is compatible with the observed inter-peptide hydrogen bonds, protofilament
 128 hydrophobic interactions and location of β -turns. Finally, sample treatment with TFA, which affects the hydrogen bonding,
 129 results in nanofiber dissolution and loss of the β secondary structure, with the appearance of a weak α -helix signal, a
 130 phenomenon observed also in the simulations for unstable β -nanofibers (Fig. 5). These results speak to the fact that β -
 131 nanofibers are compatible with experimental observations; however, additional analysis is required to determine the number of
 132 protofilaments that compose the PSM α 1 nanofiber.

133 **Diameter of Nanofibers**

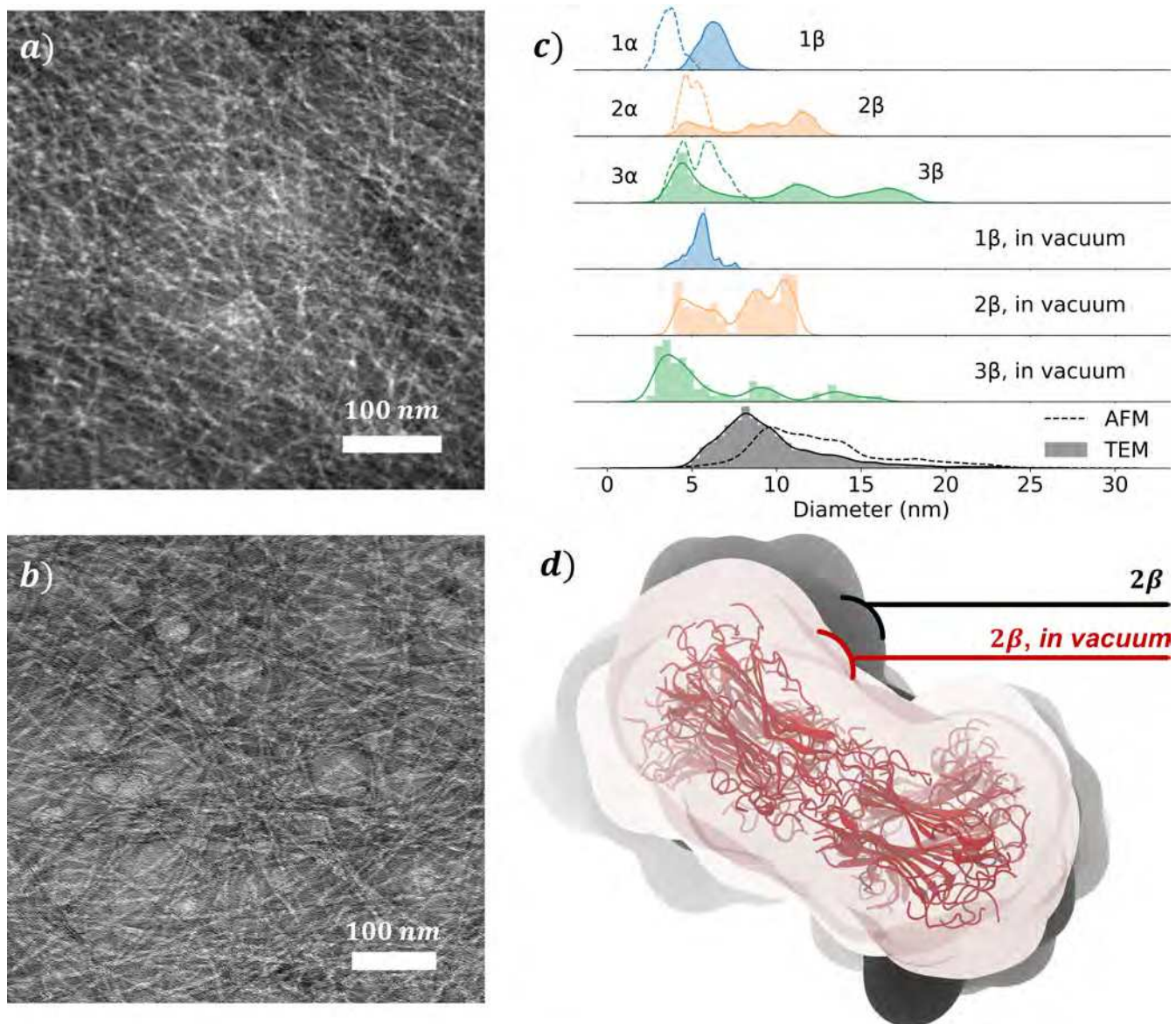


Figure 3. Nanofiber diameters. TEM images of (a) 21-day and (b) 60-day mature nanofibers. (c) Diameters from simulations for α -sheet (dotted, unfilled curves) and β -sheet (solid, filled curves) nanofibers. Distributions of PSM α 1 in solution extracted from TEM (solid, filled) and AFM (dotted, unfilled) images are shown at the bottom. (d) 2 β nanofiber volume in water (black) and in vacuum (red).

134 The nanofiber's diameter appears to be a consistent feature of both *in vivo* and *in vitro* studies^{25,26} and, therefore, a structural
 135 benchmark for our simulated structures. The experimental values for the diameter distribution of PSM α 1 nanofibers in solution
 136 slightly differs depending on the type of data used (Fig. 3a & b), showing a single broad peak and an average value of 10 nm

137 (TEM) and 12 nm (AFM). This discrepancy is likely due to the difference in sample solvation during the two measures. In
 138 order to take into account the experimental difference, we also simulated β -structures in vacuum. Of note, as mentioned before,
 139 distribution from TEM images remains largely unchanged for the mature nanofiber, with a marginal reduction of the average
 140 diameter occurring with the nanofiber aging.

141 By comparing corresponding experimental and simulated distributions (Fig. 3c), that is TEM with nanofiber in vacuum and
 142 AFM with solvated nanofiber, we can exclude the 1β system, as it peaks at shorter distances and does not show any value of
 143 the diameter above 10 nm, which are present in all the experimental distributions as well as literature data. When it comes
 144 to selecting between the 2-protofilament and 3-protofilament structures, the comparison is not as discerning; while the 3β
 145 simulated structure tends to have more frequent peaks at short range (thanks to the almost planar structure of the aggregate),
 146 the difference with experimental data is not as marked. Moreover, there are several factors that can introduce differences
 147 in the diameter distributions when obtained from experiments and simulations. First, the simulation conditions (*i.e.*, fully
 148 solvated or in vacuum) do not necessarily match the conditions of the fiber in solution. Even though the shift towards shorter
 149 diameters observed in increasing vacuum conditions (*i.e.*, AFM vs TEM) is replicated by the simulations (see Fig. 3c & d), the
 150 experimental conditions are more likely to be in an intermediate state. Second, the results from the simulations are obtained by
 151 uniformly sampling the fiber at every angle; meanwhile, this may not be possible in the experiment due to substrate, preferential
 152 direction assumed by the fiber during solvent evaporation, shape of the AFM probe, or other similar factors.

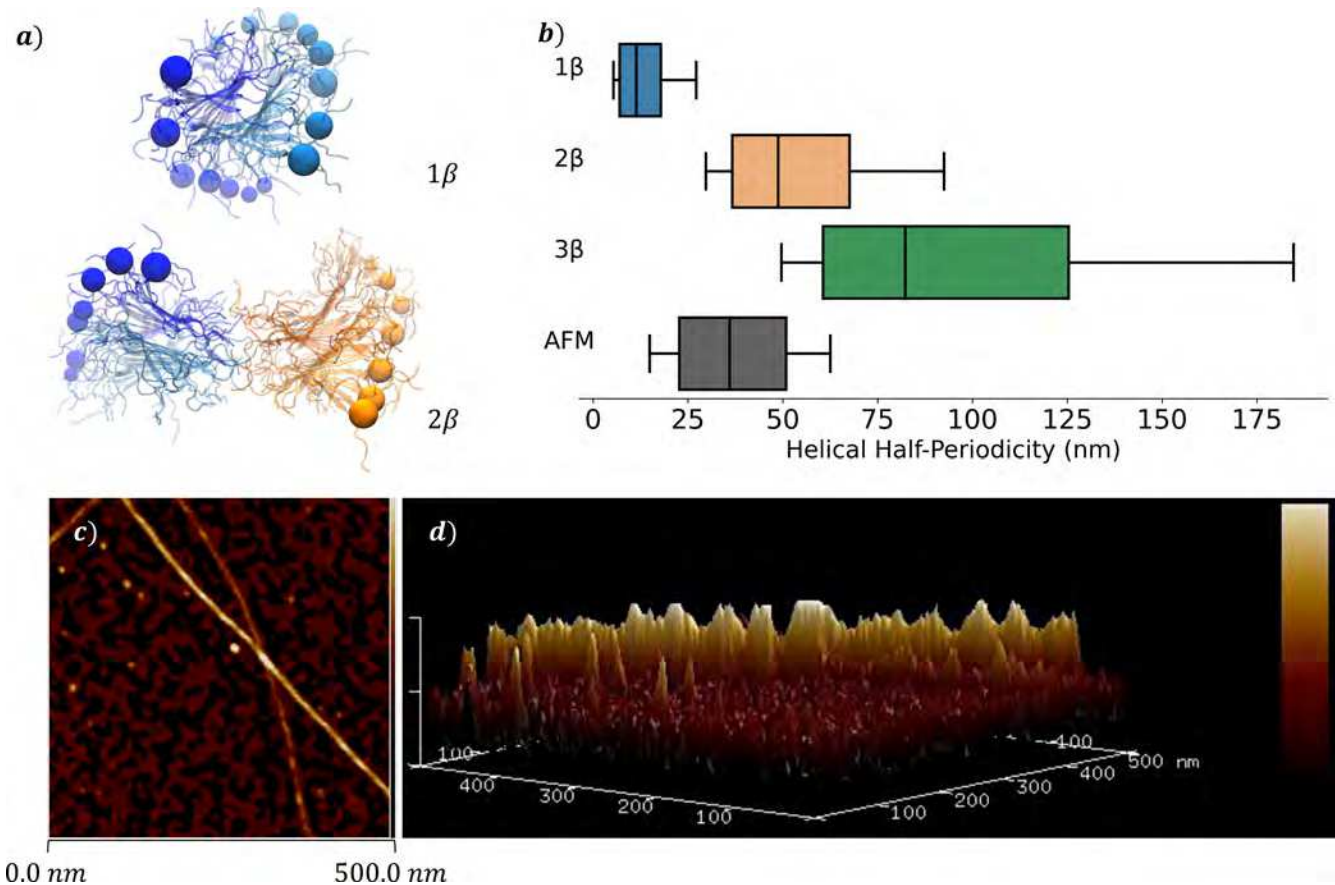


Figure 4. Helical structure of PSM α 1 nanofibers. (a) Top view of 1β and 2β nanofiber. Residues at the edge of the nanofiber were drawn with different spheres to visualize the depth effect. Some layers have been omitted for clarity. (b) β -nanofiber half-periodicity: boxes represent quartiles and whiskers delineate the 10th and 90th percentiles of the distribution. (c) AFM image of mature PSM α 1 nanofibers in aqueous solution. (d) 3D landscape corresponding to panel (c). The vertical scale bar indicates height from 0 to 7.7 nm.

153 Helicity of Nanofibers

154 As both 2β and 3β are possible candidates for the nanofiber structures in dispersion, we leveraged the differences in structure
 155 between these two classes of assembly, to determine if any (or both) structures are likely present in solution. Despite starting

from crystal-like topology, which does not resemble the structure in solvent or *in vacuo*, all the simulated β assemblies spontaneously evolve to adopt a helical configuration (Fig. 4a) over a short period of time. Moreover, all the β -nanofibers display a left-handed chirality (Fig. 4b), which matches the handedness obtained from the CD spectra of the PSM α 1 nanofibers in solution (see Fig. S3 in the SI). The quantitative comparison for the half-periodicity length (peak-to-peak intensity in the AFM image) shows that the 2-protofilament β -structure better matches the experimental results. Using the interquartile range (IQR) as an estimate of the variability (similar to the standard deviation), we found that the IQR of the AFM data (from 23 nm to 51 nm) overlaps with the IQR of the 2 β structure (from 37 nm to 68 nm), which also has a median periodicity of 49 nm. Conversely, the overlap of the experimental observation with the data for the 3 β structure is minimal.

Interestingly, the 3 β nanofibers tend to have a small layer-to-layer angle or an almost flat conformation (hence the long period), and very short fibers (10 layers, ~4 nm) prefer a right-handed chirality (this effect disappears for longer strands). This behavior, together with the low stability of the flat conformation, resulted in instability of certain lengths of 3 β nanofibers during the simulations. This observation is in contrast with the other types of aggregates that rapidly assume their helical structure when starting from flat conformation at any length.

These results suggest that the nanofiber can become locally unstable when more than two protofilaments are associated, limiting the ability of the fiber to grow laterally, and that one of the potential roles of the associated extracellular DNA observed *in vitro*³⁰ is to provide additional stability by hindering lateral growth of the nanofiber. This local instability would also explain the long time required for nanofibers in solution to reach a stable conformation (~14 days) compared to *in vitro* observations (in as few as 2 to 5 days), as lateral aggregation is still possible until most of the peptides are aggregated in a more stable nanoscale assembly. Similar phenomena have been reported before: the lateral growth of other amyloid nanofibers (A β of Alzheimer's disease, lysozyme, HET-s prion, and SAA_{1–12}, among others) due to chiral-specificity has been previously observed^{47–50}, with some studies proposing that amyloid nanofibers have exclusively left-handed chirality, although this hypothesis has been, by now, disproved^{13,24}.

The chirality reversal observed for the very short 3 β strands during the simulations elude to the possibility of other structures assuming a right-handed conformation. To this end, as we did not observe their spontaneous formation, we directly tested the stability of these structures by taking stable conformation (left-handed nanofiber, D-peptides) and either (1) inverting the chirality of the nanofiber (*i.e.*, right-handed helix) leaving peptide chirality unaltered (flipped nanofiber) or (2) inverting the chirality of both fiber and peptides (mirrored nanofiber). The results, shown in Table 1, indicate that both flipped and mirrored systems are unstable (with the notable exception of 1 β formed by L-peptides). The instability did not stem from a simple disaggregation of protofilament or strands, but rather, as shown in Fig. 5, by a complete loss of the β -sheet structure of each peptide, starting at the hydrophilic, randomly-coiled regions of the fiber and propelling toward the steric zippers at the center of the protofilaments.

Conclusions and prospective

PSM-derived functional amyloids are highly-ordered nanofibers that play a variety of important roles in the ECM of *S. aureus* biofilms. We determined the molecular structure of PSM α 1-derived nanofibers and their characteristics, leveraging a combination of atomistic simulations and experiments, including mass spectroscopy, CD spectroscopy, TEM, and AFM.

Table 1. PSM α 1 nanofiber simulations and their stability (Ⓐ stable, Ⓣ unstable). n_{proto} is the number of protofilaments; ρ_{lin} is the linear density along the nanofiber axis in kDa nm^{−1}.

Class	n_{proto}	Type	ρ_{lin}	Ref. ¹	Vac. ²	Flip. ³	Mirror. ⁴
1 β	1	β	9.55 ± 0.05	Ⓐ	Ⓐ	⊗	Ⓐ
2 β	2	β	19.48 ± 0.22	Ⓐ	Ⓐ	⊗	⊗
3 β	3	β	29.15 ± 0.21	Ⓐ	Ⓐ	⊗	⊗
1 α	1	α	4.88 ± 0.01	Ⓐ	Ⓐ	⊗	⊗
2 α	2	α	6.83 ± 0.15	Ⓐ	Ⓐ	⊗	⊗
3 α	3	α	9.88 ± 0.14	Ⓐ	Ⓐ	⊗	⊗

¹ Reference systems in water; D-peptides. ² Same as the reference systems, but in vacuum. ³ Flipped configuration: fiber chirality is inverted; D-peptides. ⁴ Mirror configuration: fiber and peptide chirality are inverted (L-peptides).

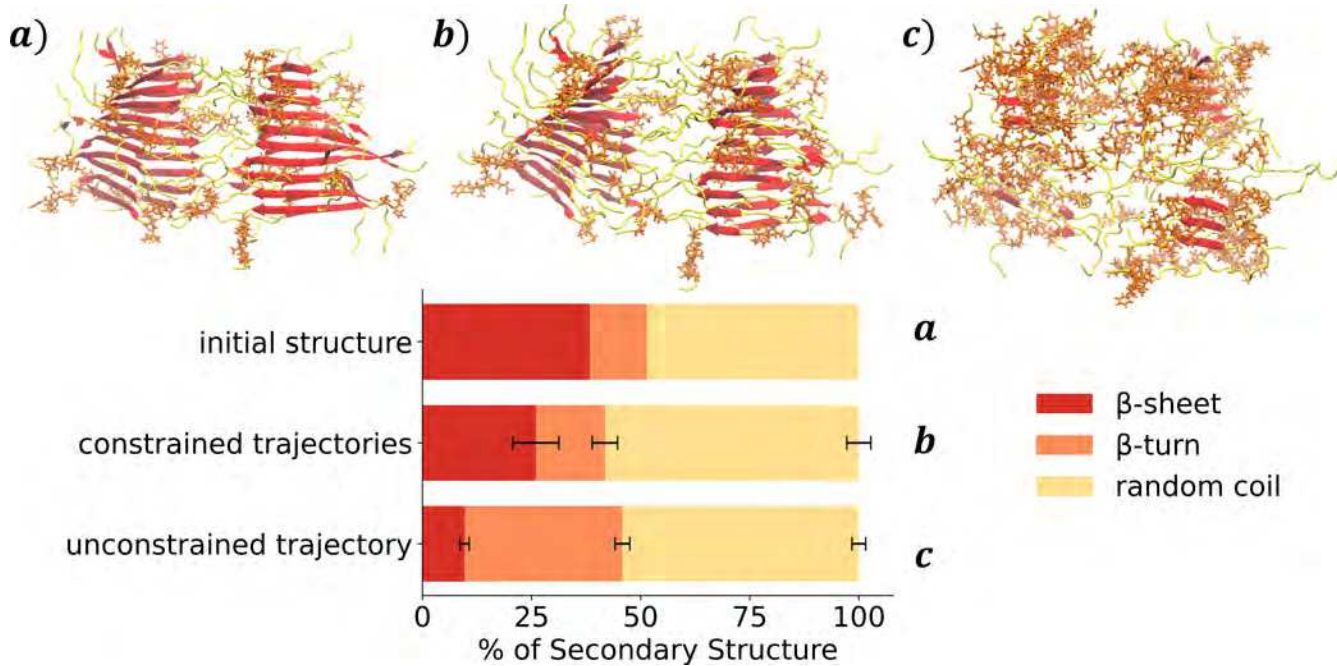


Figure 5. Dissolution of a flipped (R-chiral) 2β nanofiber and its secondary structure. Starting (a) from the flipped 2β configuration, (b) the restraints on the R-chiral nanofiber are gradually removed and (c) the system is then simulated without restraints. Error bars represent standard deviation.

PSM α 1 peptides in solution assemble into cross- β -sheet structures that spontaneously adopt a left-handed helical structure, with an average diameter of about 12.5 nm and a periodicity of \sim 72 nm. These nanoscale assemblies are stable to thermal and sonication stress, but can be partially (using HIFIP) or fully dissolved (using TFA) by treating the solution with surfactants. The characteristics of the nanofibers, match closely a structure composed of two protofilaments where β -sheet peptides form strands *via* intermolecular hydrogen bonds and pairs of strands form protofilaments largely by virtue of a hydrophobic steric zipper. The aggregation of protofilaments is stabilized by Coulomb interactions in a disordered region composed by the random coils of the protofilament peptides.

In the absence of external factors, PSM-derived nanofibers show a longer time to stabilize than previously reported: even though fibers are clearly formed after 4 to 9 days, they continue undergoing small, but detectable, changes for about 2 weeks. This time evolution might be the consequence of the slow equilibration of the aggregates towards a two-protofilament structure, a process that in *in vitro* and *in vivo* is probably aided by other constituents in the ECM (*e.g.*, extracellular DNA).

The number of protofilaments in the nanofibers affects the chirality and the stability of the structures. Three-protofilament aggregates are the most striking example of this phenomenon: while longer fibers (20 layers) form left-handed helices, short ones (10 layers) assume the opposite chirality. We were unable to simulate nanofibers with intermediate lengths, due to their instability. We speculate that, as short protofilaments are formed, the addition of a third strand causes either strain or instability for the structure, resulting in partial dissolution or fiber breakage. This process of destabilization can potentially be responsible for the extremely slow equilibration time observed in solution, and it may represent an additional reason why extracellular DNA is associated with the PSM α 1 nanofibers in biofilms. The extracellular DNA, besides concentrating the peptides, can potentially guide the chirality of the nanofiber, promoting the aggregation of two protofilaments, while hindering additional lateral growth or speeding up the recovery when a partial disaggregation occurs.

The results of this work provide insights on the properties and characteristics of PSM-derived amyloids and can aid in the design of anti-amyloids compounds with nanoscale dimensions exemplified by chiral nanoparticles⁴⁴. MD simulations can be used as a tool to assist in exploratory research aimed at unravelling the cross-binding of fibers, inhibiting or reversing protein aggregation, and they may be an important tool when it comes to optimizing prospective nanomedicine candidates in the future.

References

- Costa, E., Silva, S., Tavaria, F. & Pintado, M. Study of the effects of chitosan upon streptococcus mutans adherence and biofilm formation. *Anaerobe* **20**, 27–31 (2013).

- 218 2. Wingender, J. *et al.* Biofilms: an emergent form of bacterial life. *Nat. Rev. Microbiol* **14**, 563–575 (2016).
- 219 3. Dragos, A. & Kovacs, A. January 2017. *The peculiar functions bacterial extracellular matrix. Trends Microbiol doi* **10**
220 (11).
- 221 4. Flemming, H.-C. & Wingender, J. Relevance of microbial extracellular polymeric substances (epss)-part i: Structural and
222 ecological aspects. *Water science technology* **43**, 1–8 (2001).
- 223 5. Steinberg, N. & Kolodkin-Gal, I. The matrix reloaded: how sensing the extracellular matrix synchronizes bacterial
224 communities. *J. bacteriology* **197**, 2092–2103 (2015).
- 225 6. Branda, S. S., Vik, Å., Friedman, L. & Kolter, R. Biofilms: the matrix revisited. *Trends microbiology* **13**, 20–26 (2005).
- 226 7. Li, W. *et al.* Insights into the role of extracellular dna and extracellular proteins in biofilm formation of vibrio para-
227 haemolyticus. *Front. Microbiol.* **11**, 813 (2020).
- 228 8. Chapman, M. R. *et al.* Role of escherichia coli curli operons in directing amyloid fiber formation. *Science* **295**, 851–855
229 (2002).
- 230 9. Romero, D., Aguilar, C., Losick, R. & Kolter, R. Amyloid fibers provide structural integrity to bacillus subtilis biofilms.
231 *Proc. Natl. Acad. Sci.* **107**, 2230–2234 (2010).
- 232 10. Nicastro, L. & Tükel, Ç. Bacterial amyloids: the link between bacterial infections and autoimmunity. *Trends microbiology*
233 **27**, 954–963 (2019).
- 234 11. Hufnagel, D. A., Tükel, Ç. & Chapman, M. R. Disease to dirt: the biology of microbial amyloids. *PLoS pathogens* **9**,
235 e1003740 (2013).
- 236 12. Dueholm, M. S. *et al.* Functional amyloid in pseudomonas. *Mol. microbiology* **77**, 1009–1020 (2010).
- 237 13. Marinelli, P., Pallares, I., Navarro, S. & Ventura, S. Dissecting the contribution of staphylococcus aureus α -phenol-soluble
238 modulins to biofilm amyloid structure. *Sci. reports* **6**, 1–13 (2016).
- 239 14. Eisenberg, D. S. & Sawaya, M. R. Structural studies of amyloid proteins at the molecular level. *Annu. review biochemistry*
240 **86**, 69–95 (2017).
- 241 15. Dueholm, M. S., Albertsen, M., Otzen, D. & Nielsen, P. H. Curli functional amyloid systems are phylogenetically
242 widespread and display large diversity in operon and protein structure. *PloS one* **7**, e51274 (2012).
- 243 16. Olsén, A., Jonsson, A. & Normark, S. Fibronectin binding mediated by a novel class of surface organelles on escherichia
244 coll. *Nature* **338**, 652–655 (1989).
- 245 17. Ghrayeb, M., Hayet, S., Lester-Zer, N., Levi-Kalisman, Y. & Chai, L. Fibrilar polymorphism of the bacterial extracellular
246 matrix protein tasa. *Microorganisms* **9**, 529 (2021).
- 247 18. Van Hal, S. J. *et al.* Predictors of mortality in staphylococcus aureus bacteremia. *Clin. microbiology reviews* **25**, 362–386
248 (2012).
- 249 19. Kourtis, A. *et al.* Emerging infections program mrsa author group: Vital signs: Epidemiology and recent trends in
250 methicillin-resistant and in methicillin-susceptible staphylococcus aureus bloodstream infections-united states. *MMWR
251 Morb Mortal Wkly Rep* **68**, 214–219 (2019).
- 252 20. Cusumano, J. A. *et al.* Staphylococcus aureus bacteremia in patients infected with covid-19: a case series. In *Open forum
253 infectious diseases*, vol. 7, ofaa518 (Oxford University Press US, 2020).
- 254 21. Cheung, G. Y., Joo, H.-S., Chatterjee, S. S. & Otto, M. Phenol-soluble modulins—critical determinants of staphylococcal
255 virulence. *FEMS microbiology reviews* **38**, 698–719 (2014).
- 256 22. Peschel, A. & Otto, M. Phenol-soluble modulins and staphylococcal infection. *Nat. Rev. Microbiol.* **11**, 667–673 (2013).
- 257 23. Periasamy, S. *et al.* How staphylococcus aureus biofilms develop their characteristic structure. *Proc. Natl. Acad. Sci.* **109**,
258 1281–1286 (2012).
- 259 24. Salinas, N., Colletier, J.-P., Moshe, A. & Landau, M. Extreme amyloid polymorphism in staphylococcus aureus virulent
260 psm α peptides. *Nat. communications* **9**, 1–9 (2018).
- 261 25. Schwartz, K. & Boles, B. R. Microbial amyloids—functions and interactions within the host. *Curr. opinion microbiology*
262 **16**, 93–99 (2013).
- 263 26. Schwartz, K., Syed, A. K., Stephenson, R. E., Rickard, A. H. & Boles, B. R. Functional amyloids composed of phenol
264 soluble modulins stabilize staphylococcus aureus biofilms. *PLoS pathogens* **8** (2012).

- 265 27. Fitzpatrick, A. W. *et al.* Atomic structure and hierarchical assembly of a cross- β amyloid fibril. *Proc. Natl. Acad. Sci.* **110**,
266 5468–5473 (2013).
- 267 28. Shammas, S. L. *et al.* Perturbation of the stability of amyloid fibrils through alteration of electrostatic interactions. *Biophys.
268 journal* **100**, 2783–2791 (2011).
- 269 29. Greenwald, J. & Riek, R. Biology of amyloid: structure, function, and regulation. *Structure* **18**, 1244–1260 (2010).
- 270 30. Schwartz, K., Ganesan, M., Payne, D. E., Solomon, M. J. & Boles, B. R. Extracellular dna facilitates the formation of
271 functional amyloids in staphylococcus aureus biofilms. *Mol. microbiology* **99**, 123–134 (2016).
- 272 31. Bleem, A., Francisco, R., Bryers, J. D. & Daggett, V. Designed α -sheet peptides suppress amyloid formation in
273 staphylococcus aureus biofilms. *NPJ Biofilms Microbiomes* **3**, 1–10 (2017).
- 274 32. Schwartz, K. *et al.* The agrd n-terminal leader peptide of staphylococcus aureus has cytolytic and amyloidogenic properties.
275 *Infect. immunity* **82**, 3837–3844 (2014).
- 276 33. Syed, A. K. & Boles, B. R. Fold modulating function: bacterial toxins to functional amyloids. *Front. microbiology* **5**, 401
277 (2014).
- 278 34. Cheng, C. W. H., Chung, M. W. H. & Ng, J. C. F. Structural dynamics of amyloid- β aggregation in alzheimer's disease:
279 Computational and experimental approaches. *J. Young Investig.* **31** (2016).
- 280 35. Carballo-Pacheco, M. & Strodel, B. Advances in the simulation of protein aggregation at the atomistic scale. *The journal
281 physical chemistry B* **120**, 2991–2999 (2016).
- 282 36. Morriss-Andrews, A. & Shea, J.-E. Computational studies of protein aggregation: methods and applications. *Annu. review
283 physical chemistry* **66**, 643–666 (2015).
- 284 37. Stroud, J. C., Liu, C., Teng, P. K. & Eisenberg, D. Toxic fibrillar oligomers of amyloid- β have cross- β structure. *Proc.
285 Natl. Acad. Sci. United States Am.* **109**, 7717–7722, DOI: [10.1073/pnas.1203193109](https://doi.org/10.1073/pnas.1203193109) (2012).
- 286 38. Pan, K.-M. *et al.* Conversion of alpha-helices into beta-sheets features in the formation of the scrapie prion proteins. *Proc.
287 Natl. Acad. Sci.* **90**, 10962–10966 (1993).
- 288 39. DeBenedictis, E., Ma, D. & Keten, S. Structural predictions for curli amyloid fibril subunits csga and csgb. *RSC advances*
289 **7**, 48102–48112 (2017).
- 290 40. Andreasen, M. *et al.* Physical determinants of amyloid assembly in biofilm formation. *Mbio* **10**, e02279–18 (2019).
- 291 41. Dunbar, M., DeBenedictis, E. & Keten, S. Dimerization energetics of curli fiber subunits csga and csgb. *npj Comput.
292 Mater.* **5**, 1–9 (2019).
- 293 42. Nasica-Labouze, J. *et al.* Amyloid β protein and alzheimer's disease: When computer simulations complement experimental
294 studies. *Chem. reviews* **115**, 3518–3563 (2015).
- 295 43. Paparcone, R. & Buehler, M. J. Microscale structural model of alzheimer a β (1–40) amyloid fibril. *Appl. Phys. Lett.* **94**,
296 243904 (2009).
- 297 44. Wang, Y. *et al.* Anti-biofilm activity of graphene quantum dots via self-assembly with bacterial amyloid proteins. *ACS
298 nano* **13**, 4278–4289 (2019).
- 299 45. Jackson, M. P. & Hewitt, E. W. Why are functional amyloids non-toxic in humans? *Biomolecules* **7**, 71 (2017).
- 300 46. Tayeb-Fligelman, E. *et al.* The cytotoxic staphylococcus aureus psm α 3 reveals a cross- α amyloid-like fibril. *Science* **355**,
301 831–833 (2017).
- 302 47. Gong, S. *et al.* Unravelling the mechanism of amyloid-b peptide oligomerization and fibrillation at chiral interfaces †.
303 *Chem. Commun* **55**, 13725–13728, DOI: [10.1039/c9cc06980a](https://doi.org/10.1039/c9cc06980a) (2019).
- 304 48. Kurouski, D. *et al.* Is Supramolecular Filament Chirality the Underlying Cause of Major Morphology Differences in
305 Amyloid Fibrils? *J. Am. Chem. Soc.* DOI: [10.1021/ja407583r](https://doi.org/10.1021/ja407583r) (2014).
- 306 49. Dzwolak, W. Chirality and chiroptical properties of amyloid fibrils. *Chirality* **26**, 580–587 (2014).
- 307 50. Rubin, N., Perugia, E., Goldschmidt, M., Fridkin, M. & Addadi, L. Chirality of amyloid suprastructures. *J. Am. Chem. Soc.*
308 **130**, 4602–4603 (2008).

309 **Methods**

310 **Peptide preparation and fibrillation**

311 PSM α 1 (MGIIAGIIKVIKSLIEQFTGK) with a purity greater than 90% was purchased from ChinaPeptides (Shanghai,
312 China). Peptides were dissolved to a final concentration of 0.5 g L⁻¹ in a 1:1 mixture of trifluoroacetic acid (TFA) and
313 hexafluoroisopropanol (HFIP), followed by sonication for 10 min and incubation for 1 h at room temperature. Stock solutions
314 were divided into aliquots, solvent TFA/HFIP was dried with a Savant SpeedVac Vacuum Concentrator (Thermo Scientific,
315 USA) at room temperature, and stored at -80 °C. This preparation yielded phenol soluble modulins in monomeric form. To
316 start the fibrillation process, stored peptides were suspended in anhydrous dimethyl sulfoxide (5%) and sonicated for 10 min.
317 These peptide aliquots were then prepared in ultrapure water yielding a final peptide concentration of 200 μM for fibrillation at
318 room temperature.

319 **Nanofiber thermal and sonic stability**

320 The thermal and sonic stability of mature PSM α 1 nanofibers was tested using the following three procedures. A sonication
321 bath (FisherbrandTM) was used at operating frequency of 37 Hz to sonicate the incubated solution for 10 min, 30 min and
322 60 min. Thermal stability of the nanofibers was tested by heating the incubated solution in an oven at 37 °C and 60 °C for 1 h.
323 Furthermore, an already-heated solution was sonicated for another 1 h.

324 **Mass Spectroscopy (MS)**

325 MS was used to confirm the size of the subunits of the nanofibers. PSM α 1 nanofibers in the incubation solution were measured
326 using Bruker AutoFlex Speed matrix-assisted laser desorption/ionization-time of flight (MALDI-TOF) in both Linear and
327 Reflectron modes. PSM α 1 fibrillated for 21 d and 35 d was diluted to a concentration of 20 μM. 10 μL of a diluted sample was
328 used for MS measurement.

329 **Defibrillation in vitro**

330 TFA is an excellent solvent for most peptides, and it is commonly used in both solid- and solution-phase peptide synthesis.
331 TFA is strong proton donor capable of breaking up intra- and inter-molecular hydrogen bonding, as well as removing many
332 protecting groups and the crude synthesized peptide from resins, but it is not strong enough to cleave peptide bonds.

333 As a solvent HFIP is polar and exhibits strong hydrogen bonding properties enabling it to dissolve substances that serve
334 as hydrogen-bond acceptors, such as amides and ethers. Thus, HFIP disrupts hydrophobic forces and breaks down β-sheet
335 structures in aggregated amyloid preparations, yielding a dense, homogenous solution of monomers. Post-maturation (30 d and
336 65 d) PSM α 1 nanofibers were treated with TFA or HFIP to induce the dilapidation or defibrillation of the mature nanofibers by
337 breaking hydrogen bonding or hydrophobic forces respectively.

338 **Transmission Electron Microscopy (TEM)**

339 The TEM employed in the characterization is a JEOL 2010F Analytical Electron Microscope. Carbon-coated 400 mesh copper
340 TEM grids were placed coated-side-down for 60 s onto sample drops (10 μL) of PSM α 1 solution. The grids were then retrieved
341 and washed with deionized water (two droplets). The sample was stained with 1% (w/v) uranyl acetate for 40 s. Grids were
342 then blotted and air-dried before imaging.

343 **TEM image processing**

344 The nanofiber diameter distribution from TEM data was obtained with in-house code. The images were processed using kernel
345 filtering to determine the direction of the nanofiber in the frame of the image; we used 180 100×100 kernels for an angular
346 resolution of 1° after filtering the images to maximize the contrast between the edges and center of the nanofibers. Then, we
347 searched each filtered image in the direction perpendicular to the applied filter angle and estimated the diameter from the
348 distance between two consecutive high-contrast peaks.

349 **Atomic Force Microscopy (AFM)**

350 Matured nanofibers at three different time stages were imaged on an Innova AFM (Bruker) operated in the tapping mode.
351 Aliquots of 20 μL were deposited on freshly cleaved, buffer-washed muscovite mica (Grade V-4 mica from SPI, PA). The
352 samples were incubated for 1 min and dried under a gentle stream of nitrogen for 5 min before scanning. The images were
353 processed and analyzed using NanoScope software 6.13.

354 **AFM image processing**

355 The nanofiber periodicity and diameter distribution from ADF data was obtained with in-house code. The periodicity of the
356 PSM α 1 structure was determined from AFM images by computing the distance between highest-intensity nanofiber peaks.
357 The AFM images were initially split in multiple images, each containing a single nanofiber, to obtain relatively consistent
358 intensity ranges. The highest point in the nanofibers where then identified using the Otsu thresholding method and the distance

359 between the center of closest peaks was collected. As the distance is dependent upon the Otsu threshold parameter, which in
360 turn depends on the intensity of the pixel, the threshold parameter for each image was determined to be the value, between 1.1
361 and 3.1, that minimizes the standard deviation for the values of the distances between the regions of highest intensity. Diameters
362 were obtained by first segmenting images in order to separate the fiber from the background. 3000 to 5000 points in the fiber
363 were then randomly chosen and, for each of them, the diameter was set equal to the shortest distance to opposite edges, which
364 was found by sampling all the directions with a 1° resolution.

365 **Molecular Dynamics Simulations**

366 All simulations were performed with a combination of Nanoscale Molecular Dynamics (NAMD) and PLUMED software,
367 using explicit TIP3P water and the all-atom force field CHARMM, version 36. A time step of 1 fs or 2 fs was employed to
368 integrate the equations of motion, and hydrogen atoms are kept rigid via the SHAKE algorithm. Nonbonded short-range
369 interactions smoothly approached 0 using an X-PLOR switching function between 1 nm and 1.2 nm, in conjunction with the
370 particle mesh Ewald algorithm to evaluate long-range Coulombic forces. A Langevin thermostat, with a time constant of 1 ps,
371 was used to keep the temperature constant at 310 K. The systems were minimized for 1000 steps before the equilibration runs,
372 and equilibrated using a PLUMED harmonic restraint between peptides. Equilibration simulations were performed, first, in
373 canonical ensemble with and without restraints, during which time the harmonic restraints between peptides were gradually
374 set to zero, followed by simulations in the aniso-(NPT) ensemble. Finally, unrestrained nanofibers were run in the canonical
375 ensemble until the root mean squared deviation of the nanofibers plateaued for at least 40 ns. Visual Molecular Dynamics and
376 the MDAnalysis Python library were used for visualization and data analysis, respectively. For the *in vacuo* simulations, the
377 N- and C-termini and charged amino acid groups (*i.e.*, LYS and GLU) were neutralized by adding or removing proton atoms.
378 Simulations of nanofibers with a chirality (Flipped and Mirror) different from the one spontaneously assumed during simulation
379 (Reference), were prepared in two ways: (1) inverting the chirality of the nanofiber but leaving the chirality of each peptide
380 untouched (Flipped), and (2) taking the mirror image of the nanofiber, such that the nanofiber chirality and the chirality of
381 each peptide are inverted (Mirror). These simulations were generated from the configuration equilibrated as described above;
382 however, after the chirality is changed, an additional NPT relaxation was performed by applying harmonic constraints that
383 restrained the alpha carbons and hydrogens that were gradually tapered off over 15 ns.

384 **Simulation Postprocessing**

385 The diameter was computed by (1) determining the nanofiber direction (*i.e.*, nanofiber main axis), (2) dividing the nanofiber
386 with planes perpendicular to the nanofiber axis (*i.e.*, slices), (3) dividing each slice in an even number of equal sectors, and (4)
387 using the distance of the farthest atom from the nanofiber's axis of opposite sectors to sample the diameter. The nanofiber axis
388 (step 1) was determined by linear regression of atomic spatial coordinates. Then, the atoms were grouped in wedges (step 2 and
389 3) by using slices that are 1-4 nm wide and 8-20 sectors (each sector wedge covers 18° to 45° on the plane), where the selected
390 parameters for each nanofiber (*i.e.*, slice height and number of sectors) are different, depending on which combination yielded
391 the smallest standard deviation. Slice height and number of sector parameters do not impact the final diameter distribution, as
392 demonstrated in Fig. S8. To minimize edge effects, we discarded any slice that did not have at least one atom in each sector. The
393 final diameter distribution is obtained by collecting the sum of the distances of the atoms that were farthest from the nanofiber
394 axis in opposite sectors.

395 The periodicity of the PSM α 1 helical structure was determined from the average layer-to-layer angle and average layer-to-
396 layer distance projected along the nanofiber axis, determined by linear regression of all atomic coordinates. For each layer
397 (see Fig. 1), first the center of mass and the principal axes of inertia were computed, followed by the layer-to-layer distance
398 (*i.e.*, distance between the center of mass of consecutive layers) and by the layer-to-layer angle (dihedral angle from the largest
399 principal axis of each layer and the center of mass of two consecutive layers).

400 In the manuscript, we report the results obtained for the longest simulated fiber in each class, while data of shorter fibers
401 were used to test the convergence of the results, as they generally show a somewhat monotonic trend with aggregate length.
402 This effect becomes small when at least 20 layers are present even for the quantities that have the strongest dependence from
403 the nanofiber length (see Figs. S9 and S10).

404 **Acknowledgements**

405 This project was financially supported by the University of Michigan's BlueSky Initiative and by the Department of Defense
406 Advanced Research Projects Agency (DARPA), grant n. HR00111720067. We acknowledge University of Michigan's ARC-TS
407 for use of their high performance computing resources, particularly Great Lakes.

408 **Author contributions statement**

409 AV, NK, JV PE and YW conceived and designed the study. C Luyet and PE conceived and analyzed the simulations. C Luyet
410 and YW ran the simulations. C Liu, C Luyet, and PE coded the simulations and image post-processing tools. YW designed and
411 carried out the experiments. AV, C Luyet, and PE co-wrote the paper with input from all co-authors. All authors discussed the
412 results and reviewed the manuscript.

413 **Additional information**

414 All the authors declare no competing interests.

Supplementary Files

This is a list of supplementary files associated with this preprint. Click to download.

- [SINNANO22010083.pdf](#)